

Comparative study of the cavitation resistance of the traditional and high-lift hydrofoils for hydrokinetic application

Jonatan Gutiérrez, Ainhoa Rubio-Clemente, Edwin Chica*

Grupo de Investigación Energía Alternativa (GEA), Facultad de Ingeniería, Universidad de Antioquia UdeA, Calle 70 No. 52-21, Medellín 050010, Colombia

ABSTRACT


The cavitation phenomena should be considered during the design of hydrokinetic turbines due to cavitation could cause surface erosion, mechanical vibrations, undesirable noise and efficiency reduction in the energy transformation. Therefore, the aim of this work is to conduct a numerical comparison of the cavitation resistance of 3 hydrofoils (NACA0015, Eppler420 and S822) with the purpose of selecting the best foil for the blade cross-section design. For each hydrofoil, the traditional and the high-lift configurations were evaluated. The hydrodynamic factors, including the lift and the drag (C_L and C_D , respectively) coefficients were determined by using JavaFoil software for several angles of attack (α). Additionally, for the computational fluid dynamics (CFD) study in ANSYS Fluent software, the SST $k - \omega$ and the Schnerr and Sauer turbulence and cavitation models were respectively utilized to validate the values of C_L and C_D , and to calculate the pressure coefficient (C_p). The values of C_p were compared with the cavitation number (σ) for identifying cavitation on the blade and comparing the cavitation resistance of the hydrofoils studied. The methods used and the numerical results obtained were subsequently analyzed and validated using relevant experimental values available in the literature for the NACA0015 hydrofoil. CFD simulations revealed that the NACA0015 traditional hydrofoil and the high-lift configuration of the Eppler420 hydrofoil have the best resistance to cavitation inception in comparison with the traditional hydrofoils and the high-lift configurations studied, respectively.

Keywords: Schnerr and Sauer cavitation model, Hydrofoil, Cavitation, Horizontal axis hydrokinetic turbine.

OPEN ACCESS

Received: May 10, 2021
Revised: February 6, 2022
Accepted: February 19, 2022

Corresponding Author:
 Edwin Chica
edwin.chica@udea.edu.co

 **Copyright:** The Author(s). This is an open access article distributed under the terms of the [Creative Commons Attribution License \(CC BY 4.0\)](https://creativecommons.org/licenses/by/4.0/), which permits unrestricted distribution provided the original author and source are cited.

Publisher:
[Chaoyang University of Technology](https://www.chaoyang.edu.cn/)
 ISSN: 1727-2394 (Print)
 ISSN: 1727-7841 (Online)

1. INTRODUCTION

Cavitation is a hydrodynamic phenomenon that can occur on the blades of hydrokinetic turbines, since these are submerged in water currents from rivers and tidal (Gharraee et al., 2016; Jung and Kim, 2015; Wang et al., 2015; Zhang et al., 2015). This phenomenon is produced from the velocity and pressure fluctuation in the fluid around the cross-sections of the blades. Comparing the cavitation number (σ) with the minimum pressure coefficient (C_p) on the hydrofoil surface allows to predict this phenomenon. Cavitation often results in the generation and implosion of vapor bubbles near the blade surface, which alters the flow. The possible consequences of this fact on the blades are the flow-induced noise and vibration, blade surface damage caused by the erosion of the leading edge and, subsequently, a lift/thrust decrease combined with an increase of drag resulting in a performance reduction. Therefore, cavitation should be avoided during the design of blades for hydrokinetic turbines, as a consequence of the cost rise related to the reduction of the energy captured from the fluid and the turbine rotor maintenance (Amromin, 2014; Kim and Lee, 2015). The most important aspects influencing the

cavitation around a hydrofoil are the depth of immersion, the fluid conditions, the tip speed ratio, the hydrofoil shape and the surface characteristics. The vapor bubble size and shape also vary due to the action of the velocity and pressure fields (Kim and Lee, 2015).

In the literature, the cavitation was found to be avoided by using a suitable design and selecting two-dimensional (2D) sections or hydrofoils for the design of the turbine blades. These sections should have at least high hydrodynamic performance, enough thickness for structural requirement and low susceptibility to cavitation, due to the performance and lifetime of hydrokinetic turbines are mostly dependent on the shape or the geometric configuration of the hydrofoil used and the chord length and twist angle distribution along the blade. From the selected hydrofoil and by using the blade element momentum (BEM) theory, the blades of hydrokinetic turbines can be designed. Each blade is utilized to produce a lift force extracting kinetic energy from the water flow in tidal and marine currents, and rivers in order to rotate a power generator for producing electricity. There is an abundance of available literature regarding the blade design for hydrokinetic turbine considering the possibility of cavitation. The results have demonstrated that in order to design a high performance hydrokinetic turbine, C_{pre} should be as low as possible, while the lift coefficient (C_L) and the lift to drag ratio (C_L/C_D) should be as high as possible. In this regard, several families of blade sections, such as NACA, NREL, Gottingen, Eppler, Riso and Wortmann, can be used to provide a suitable blade cross-section for hydrokinetic turbines with low susceptibility to cavitation. Numerical and experimental studies have demonstrated that a number of hydrofoils of these families can provide improved cavitation performance (Amromin et al., 2006; Batten et al., 2008; Goundar et al., 2012; Sale et al., 2009; Schnerr et al., 2008; Silva et al., 2015).

More recently, various studies have been carried out aiming at showing the potential of high-lift hydrofoil configurations to increase the hydrodynamic performance of the cross-section of a wind or hydrokinetic turbine blade (Aguilar et al., 2019; Eisele and Pechlivanoglou, 2014; Gaunaa et al., 2012; Jaume and Wild, 2016; Gaunaa et al., 2013; Narsipur et al., 2021; Ragheb and Selig, 2012; Zahle et al., 2012; Yavuz et al., 2015).

The referred configurations were created by considering several combinations of flaps and slats around a main hydrofoil element. Flaps and slats were located after and before the main element, respectively (Narsipur et al., 2012; Ragheb and Selig, 2011).

In spite of the benefits of the high-lift configuration to rise the hydrodynamic performance of the hydrokinetic turbine cross-section, from the authors' knowledge, few studies have been performed to evaluate the cavitation in high-lift hydrofoil configurations for hydrokinetic application. Therefore, this work describes the hydrodynamic characteristics of 3 hydrofoils used for

hydrokinetic turbines. The pressure distribution of the hydrofoil, the minimum C_p the C_L and C_D coefficients and the C_L/C_D for the high-lift and the traditional configurations are numerically analyzed and compared with each other by using the JavaFoil numerical code and the ANSYS Fluent software. The methods used and the numerical results obtained are validated with experimental data available in the literature.

2. NUMERICAL MODELING

2.1 Hydrodynamic Analysis in JavaFoil Code

The numerical comparison of the cavitation resistance of 3 hydrofoils, including NACA0015, Eppler420 and S822, were performance by using the JavaFoil code and the ANSYS Fluent software. Table 1 shows the main characteristics of each hydrodynamic hydrofoil evaluated.

In the JavaFoil code, for the high-lift and traditional configurations, the relationship between the hydraulic parameters, such as C_L and C_D coefficients of the hydrofoils with angles of attack (α), has been observed. The Reynolds number (Re) of 750000, which is typical for hydrokinetic turbines, was used to analyze the hydrofoils studied. The chord length (C) was set at 1 in the traditional and the high-lift hydrofoil configurations for the numerical analysis. In turn, C_L and C_D were evaluated every 1° in a α range comprised from -5° to 20° . For the analysis of the high-lift configuration, a hydrofoil-flap arrangement was employed. This configuration consists of a flap located behind the trailing edge of a main hydrofoil, as it is illustrated in Fig. 1. C_1 was the chord length of the main element. On the other hand, the flap chord length was 30% of C_1 , following the guidelines given by Narsipur et al. (2012). The vertical space (d) between elements was 3% of the C_1 length, and the horizontal space (h) between the leading and the trailing edges of the second and main elements, respectively, was close to 5% of C_1 . Finally, the deflection angle (δ) was ranged from 10 to 50° during the 2D hydrodynamic analysis in the JavaFoil software in order to obtain the optimal hydrofoil configuration. During the numerical analysis, α and δ were defined based on the maximum value of C_L .

2.2 Hydrodynamic Analysis in Ansys Fluent

The flow field around of hydrofoils under the cavitation phenomenon for the high-lift and traditional configurations, as well as the C_L , C_D and C_p values, were calculated by CFD simulations, which were conducted through ANSYS Fluent Software. C_L , C_D and C_p were defined as expressed by Equation (1), (2) and (3) respectively.

$$C_L = \frac{1}{\frac{1}{2}\rho_\infty U_\infty^2} \int_S F_{\perp U_\infty} dS \quad (1)$$

$$C_D = \frac{1}{\frac{1}{2}\rho_\infty U_\infty^2} \int_S F_{\parallel U_\infty} dS \quad (2)$$

Table 1. Geometrical characteristics of the hydrodynamic hydrofoils studied. Source: <http://airfoiltools.com>

| Hydrofoil | Developer | Maximum thickness | Maximum thickness location | Maximum chamber | Maximum chamber location |
|-----------|--|-------------------|----------------------------|-----------------|--------------------------|
| S822 | NREL | 16.0% | 39.2% | 1.8% | 59.5% |
| Eppler420 | Dr. Richard Eppler | 14.3% | 22.8% | 10.6% | 40.5% |
| NACA0015 | National Advisory Committee for Aeronautics (NACA) | 15.0% | 30.0% | 0.0% | 0.0% |

Percentage with respect to the chord length

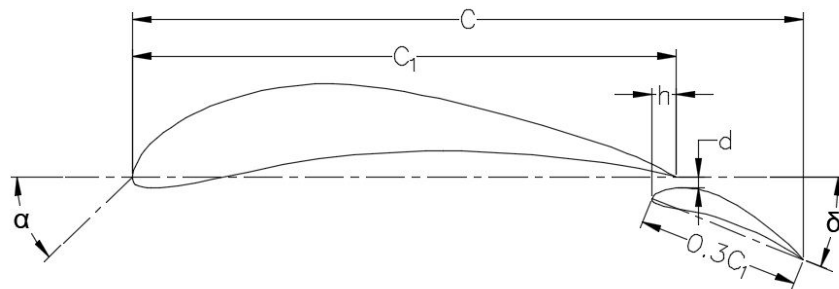


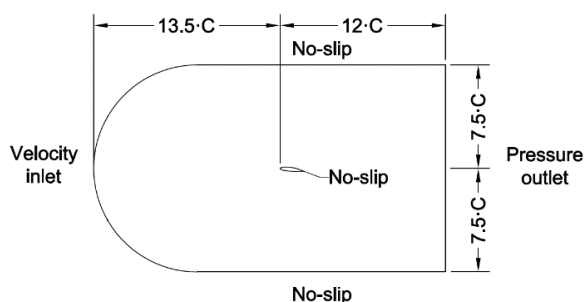
Fig. 1. Schematic hydrofoil-flap arrangement

$$C_p = \frac{P_L - P_\infty}{\frac{1}{2}\rho V_{Rel}^2} \quad (3)$$

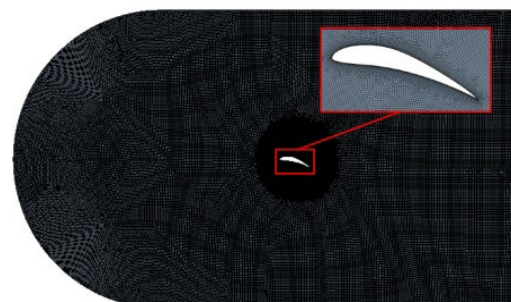
where ρ and U_∞ are the density and velocity of the fluid, respectively; S refers to the hydrofoil surface; $F_{\perp U_\infty}$ is a component of the fluid dynamic force orthogonal to the upward flow direction, F_{\parallel} is the component of the fluid dynamic force in the upward flow direction, where P_L is the local pressure, V_{Rel} is the relative velocity and P_∞ refers to the absolute pressure or the freestream static pressure, which is defined as $P_\infty = P_A + \rho gh$, being P_A the atmospheric pressure; g refers to the gravitational acceleration and h is the distance between the hub center and the free water surface. The product among p , g and h is so called as the gauge pressure.

The hydrokinetic turbine blade design is based on the BEM theory for calculating the twist angle and the chord distributions. In this study, C and the relative velocity (V_{Rel}) were 0.1773 m and 5.517 m/s, respectively. The Eppler420 hydrofoil was used as the reference hydrofoil to show the computational domain. This hydrofoil has the lower thickness of the hydrofoils studied. The hydrofoils were

placed within the computational domain at the α resulting in the highest C_{LMax}/C_D . The values of α were 17° , 12° and 5° for the Eppler420, S822 and NACA0015 traditional hydrofoil configurations, respectively. For the high-lift hydrofoil configuration the values of α were 8° , 7° and 9° for the Eppler420, S822 and NACA0015 hydrofoils, respectively. Additionally, for these geometrical configurations, the values of δ were 30° , 20° and 10° for the Eppler420, S822 and NACA0015 hydrofoils, respectively. For the numerical simulation, the computational domain used in these studied has a C-Topology; therefore, the mesh consisted of a rectangular grid of $18C$ of length and a semicircle grid of $7.5C$ of radius. The hydrofoil was placed at the center of the lower and the upper boundaries. The hydrofoil leading edge was located at $13.5C$ from the inlet boundary. The fluid used during the simulation was water at a temperature of 298.15 K. A velocity inlet in X-direction equal to 5.517 m/s was defined in C type boundary and a pressure outlet boundary was imposed at the outlet boundary. Finally, in the hydrofoil and in other boundaries, the no-slip condition was defined. The boundary conditions and the computational domain are represented in Fig. 2.



(a)



(b)

Fig. 2. a) Computational domain and boundary conditions. b) Mesh of the computational domain for the Eppler420 hydrofoil

This domain was meshed using an unstructured mesh and inflation layers were generated around the hydrofoil in order to obtain a higher computational accuracy. In addition, y^+ was less than 1 in order to meet the $k - \omega$ SST turbulence model requirements, which was employed in the numerical analysis. The mesh of the computational domain is presented in Fig. 2.

The unsteady Reynolds-Averaged-Navier-Stokes (RANS) equations were used with the $k - \omega$ SST turbulence model for the numerical simulation. The Schnerr-Sauer cavitation model was used in the set of the numerical studies for each hydrofoil due to the cavitation state can be accurately simulated by this model (Hong et al., 2016; Hong et al., 2018; Shi et al., 2021). The model of cavitation is based on the Rayleigh-Plesset cavity dynamics equation. The residual target was set at 10^{-4} . The cavitation condition was determined according to σ , which was defined in Equation (4).

$$\sigma = \frac{P_\infty - P_V}{\frac{1}{2}\rho V_{Rel}^2} \quad (4)$$

where ρ , P_∞ and P_V are the water density, the freestream static pressure and the saturation vapor pressure, respectively. In turn, P_V was fixed at 2339.26 Pa for a flow-field temperature of 298.15 K. σ was set at 4.23 in this work due to the operating pressure of 66615.84 Pa, the blade depth of 1.5 m and the water velocity of 5.517 m/s.

Once the geometry and the mesh are created, the mesh size and the time-step convergence analyses of the solution were tested considering the Richardson extrapolation, which was introduced by Roche (Roche 1994; Roche 1997). For this purpose, 3 different mesh densities and 3 time steps were used for the independence study. The grid convergence index (GCI) was used as an indicator of the mesh and the time convergence level. C_L was monitored to verify the mesh and the time step independence.

For the mesh independence study, the GCI can be obtained by means of Equation (5) when the fine mesh solution is used or by means of Equation (6), when the coarse mesh solution is used (Prakoso et al., 2019; Roche 1994; Roche 1997).

$$GCI_{fine} = \frac{F \cdot |\epsilon_1|}{r^{p-1}} \quad (5)$$

$$GCI_{coarse} = \frac{F \cdot |\epsilon_2|}{r^{p-1}} \quad (6)$$

where r is the relationship between the size of the fine mesh and the characteristic size of the medium mesh. r can also be defined as the relationship between the size of the medium mesh and the characteristic size of the coarse mesh. ϵ_1 is the solution (f) relative error estimate of a control variable (C_L), which is obtained as the difference between the fine (f_1) and the medium (f_2) solution divided by f_1 . In turn, ϵ_2 is obtained as the difference between f_2 and the coarse solution (f_3) divided by f_2 . The F term is a factor of

safety, whose value is usually taken as 3 (F is sometimes equal to 1.25, when many mesh sizes are used to estimate p , which stands for the order of convergence. p is determined as expressed in Equation (7).

$$p = \frac{\ln\left(\frac{f_3 - f_2}{f_2 - f_1}\right)}{\ln(r)} \quad (7)$$

The Richardson extrapolation defines the exact value of the studied variable as represented in Equation (8) (Prakoso et al., 2019; Roche 1994; Roche 1997).

$$f_{h=0} = f_1 + \frac{f_1 - f_2}{r^p - 1} \quad (8)$$

Lastly, I , which stands for the asymptotic range of convergence index and is expressed by Equation (9), must be analyzed to ensure that the time-step or the mesh sizes are within the convergence asymptotic range (Roche, 1994).

On the other hand, to ensure that the numerical simulation is within the asymptotic range, the values of I should approach 1. Therefore, for the independency study of the time-step and the mesh size by using GCI methods, 3 different mesh sizes and time-steps were used for each hydrofoil studied. In Table 2, a summary of the convergence analysis using a F-value of 1.25 is listed.

$$I = \frac{GCI_{coarse}}{r^p GCI_{fine}} \cong 1 \quad (9)$$

The results presented in Table 2 proved that the numerical results are independent on the time-step and mesh sizes. Thus, considering the good compromise in terms of computational time and results achieved, the medium time-step and the medium mesh were used for the set of subsequent simulations carried out here. In Figs. 3 and 4, the results from Richardson extrapolation for the time-step and the mesh independency studies, respectively, are shown.

3. RESULTS AND DISCUSSION

The comparison between the curves defined by C_L and C_L/C_D versus α for the hydrofoils obtained by the numerical method using JavaFoil software are shown in Fig. 5.

As α increases, the C_L values rise. Nonetheless, there is a α point at which the values of C_L begin to decrease. This results in the loss of the hydrofoil lift, which is related to the detachment of the fluid boundary layer. Table 3 shows the comparison of the numerical results obtained using JavaFoil and ANSYS Fluent software. For the NACA0015 traditional hydrofoil, the maximum C_{Lmax} was found when α was equal to 8° . However, this hydrofoil was also modeled when α was equal to 5° due to the experimental data used for validating the numerical results were carried out for the referred α value.

Table 2. Results from convergence analysis

| Hydrofoil | Mesh (number of elements) | C_L | Richardson extrapolation | Time-step (Δt) | C_L | Richardson extrapolation |
|-----------------------------------|---------------------------|--------|------------------------------------|--------------------------|--------|------------------------------------|
| Eppler420 | Fine (142567) | 1.0871 | GCI_{Coarse} (-0.0019) | 0.2700 | 0.9874 | GCI_{Coarse} (0.0041) |
| | Medium (115210) | 1.0849 | GCI_{Fine} (-0.0044) | 0.2900 | 0.9898 | GCI_{Fine} (0.0011) |
| | Coarse (89260) | 1.0839 | $f_{h=0}$ (1.0833) I (1.0020) | 0.3100 | 0.9989 | $f_{h=0}$ (0.9865) I (0.9976) |
| Eppler420 high-lift configuration | Fine (424030) | 2.8314 | GCI_{Coarse} (0.0149) | 1.5000 | 2.7952 | GCI_{Coarse} (-0.0086) |
| | Medium (399285) | 2.8050 | GCI_{Fine} (0.0031) | 2.0000 | 2.8202 | GCI_{Fine} (0.0198) |
| | Coarse (122552) | 2.6779 | $f_{h=0}$ (2.8383) I (1.0094) | 2.5000 | 2.8311 | $f_{h=0}$ (2.8395) I (0.9911) |
| S822 | Fine (152888) | 0.1788 | GCI_{Coarse} (-0.1098) | 0.1900 | 0.1667 | GCI_{Coarse} (-0.0592) |
| | Medium (122324) | 0.1847 | GCI_{Fine} (-0.1650) | 0.2100 | 0.1679 | GCI_{Fine} (-0.0681) |
| | Coarse (96001) | 0.1941 | $f_{h=0}$ (0.1685) I (1.0509) | 0.2300 | 0.1689 | $f_{h=0}$ (0.1758) I (0.9933) |
| S822 high-lift configuration | Fine (399834) | 1.6529 | GCI_{Coarse} (0.0070) | 0.5000 | 1.6448 | GCI_{Coarse} (-0.0016) |
| | Medium (324534) | 1.6609 | GCI_{Fine} (0.0011) | 0.6000 | 1.6430 | GCI_{Fine} (-0.0030) |
| | Coarse (249042) | 1.6077 | $f_{h=0}$ (1.6515) I (0.9952) | 0.7000 | 1.6440 | $f_{h=0}$ (1.6409) I (1.0011) |
| NACA0015 | Fine (145628) | 0.4554 | GCI_{Coarse} (-0.0092) | 0.8000 | 0.4564 | GCI_{Coarse} (-0.0120) |
| | Medium (117557) | 0.4582 | GCI_{Fine} (-0.0603) | 1.0000 | 0.4582 | GCI_{Fine} (-0.0172) |
| | Coarse (92258) | 0.4779 | $f_{h=0}$ (0.4549) I (1.0430) | 1.2000 | 0.4596 | $f_{h=0}$ (0.4627) I (0.9959) |
| NACA0015 high-lift configuration | Fine (184550) | 1.1410 | GCI_{Coarse} (0.0024) | 1.0000 | 1.1428 | GCI_{Coarse} (-0.0127) |
| | Medium (150439) | 1.1428 | GCI_{Fine} (0.0003) | 1.3000 | 1.1506 | GCI_{Fine} (-0.0214) |
| | Coarse (122878) | 1.1290 | $f_{h=0}$ (1.1407) I (0.9984) | 1.6000 | 1.1553 | $f_{h=0}$ (1.1623) I (0.9932) |

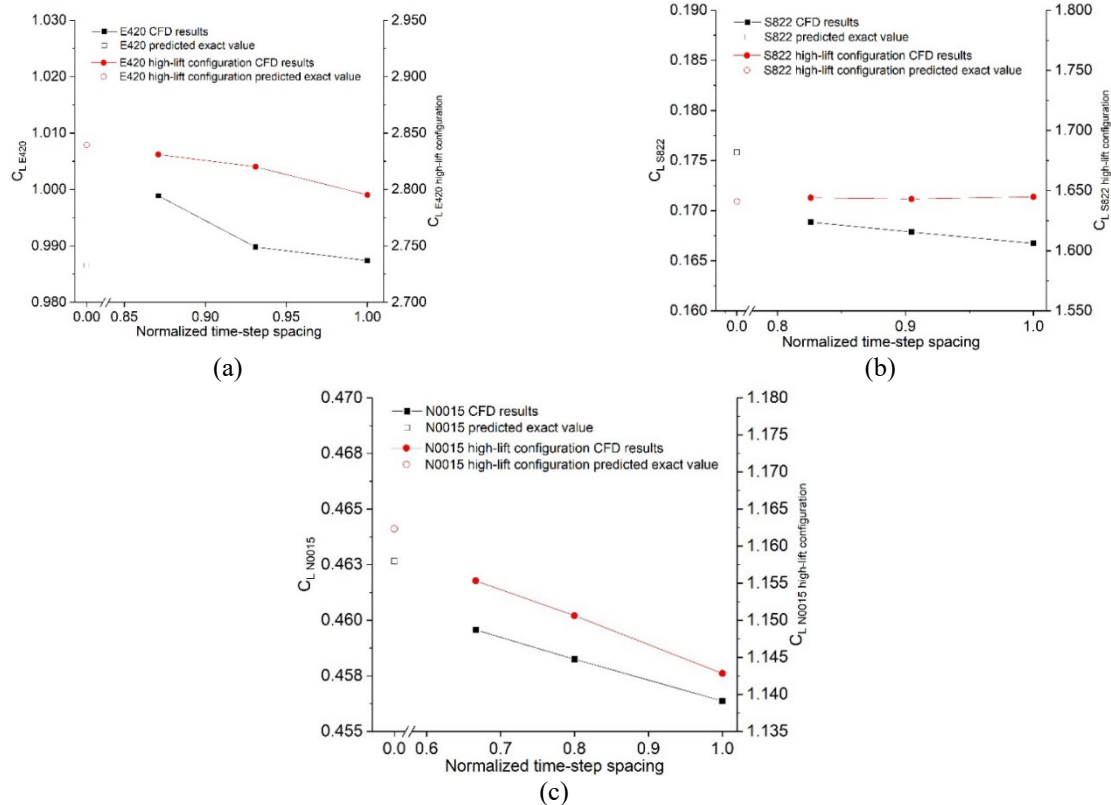


Fig. 3. Time-step independence test results: a) Eppler420 high-lift and traditional hydrofoil configurations, b) S822 high-lift and traditional hydrofoil configurations, and (c) NACA0015 high-lift and traditional hydrofoil configurations

The flow created around the hydrofoil is close to an irrotational and a non-viscous flow; i.e., an ideal flow, when α is small. Under this scenario, a weak interaction between the non-viscous and the viscous field occurs. In turn, a flow separation around the hydrofoil occurs for high α values. Therefore, the best hydrofoils were the Eppler420 traditional configuration with a α value equal to 17° , and the Eppler420 high-lift configuration with α and δ values equal to 8° and 30° , respectively, based on the comparisons of C_{Lmax} from the ANSYS Fluent results. The Eppler420 traditional hydrofoil had a C_{Lmax} (2.1106) higher than the values obtained with the other 2 hydrofoils studied.

However, the NACA0015 traditional configuration hydrofoil with a α of 5° had a higher C_{Lmax}/C_D (24.4410) than that obtained for the Eppler420 and S822 hydrofoils when the value of C_{Lmax} is achieved. In turn, the Eppler high-lift configuration hydrofoil had a higher C_{Lmax} (2.8069) compared to the other hydrofoil. Nevertheless, the NACA0015 high-lift configuration hydrofoil at a α of 5° had a higher C_{Lmax}/C_D (28.7089) compared to that one achieved for the S822 (22.8819) and the Eppler420 (26.7607) high-lift configuration hydrofoils.

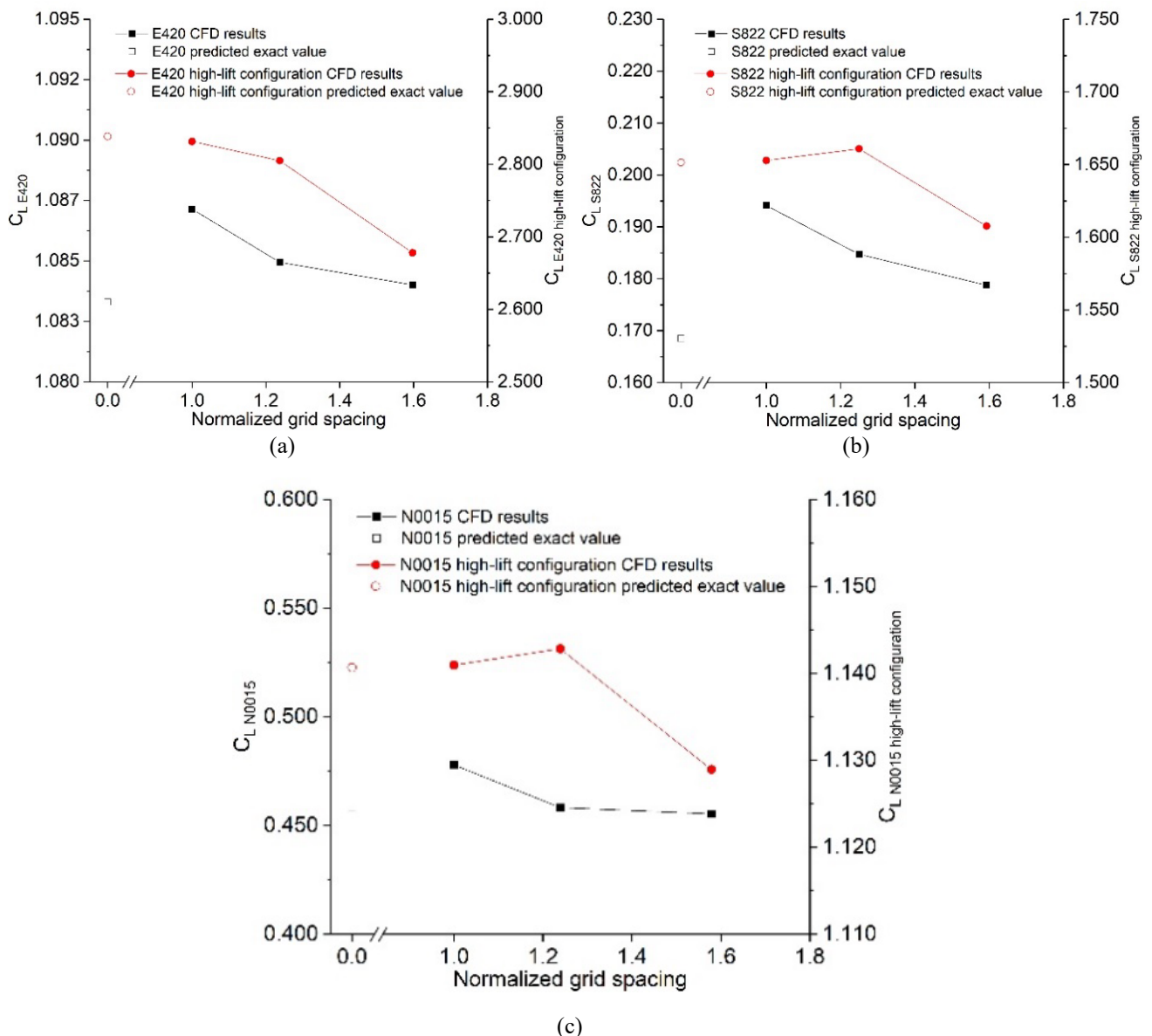


Fig. 4. Mesh independence test results: a) Eppler420 high-lift and traditional hydrofoil configurations b) S822 high-lift and traditional hydrofoil configurations, and (c) NACA0015 high-lift and traditional hydrofoil configurations

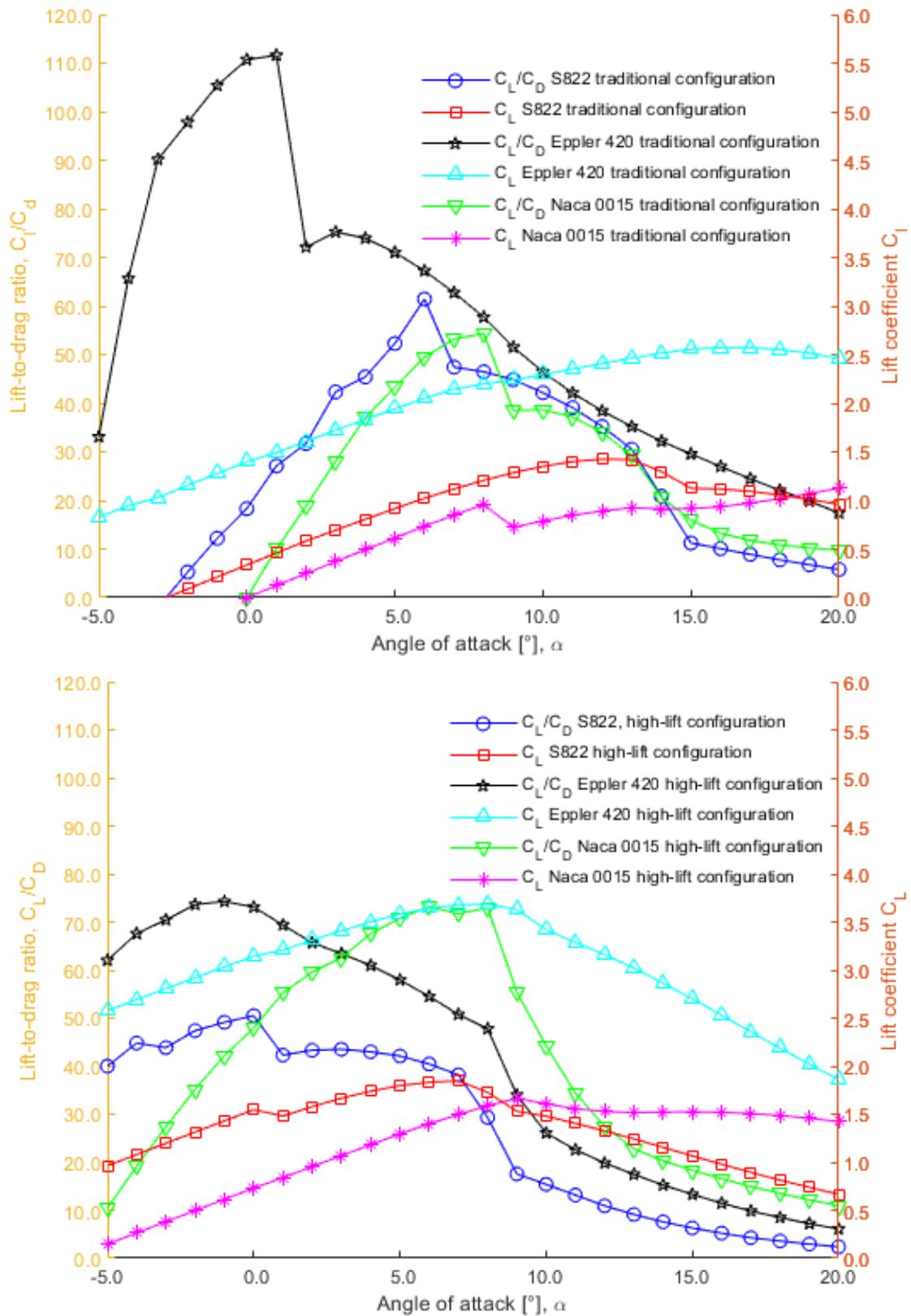


Fig. 5. Curves representing the lift-to-drag ratio (C_L/C_D) and the lift coefficient (C_L) vs. the angle of attack (α) for the high-lift and the traditional configurations

Table 3. Numerical results related to the hydrodynamic performance of the hydrofoil studied

| Hydrofoil | Parameters | JavaFoil results | ANSYSs Fluent results |
|-------------------------------------|----------------|------------------|-----------------------|
| S822 traditional configuration | α | | 12.0° |
| | C_{Lmax} | 1.4240 | 1.2074 |
| | C_D | 0.0405 | 0.0882 |
| | C_{Lmax}/C_D | 35.2040 | 13.6962 |
| S822 high-lift configuration | α | | 7.0° |
| | δ | | 20.0° |
| | C_{Lmax} | 1.8470 | 1.6555 |
| | C_D | 0.0484 | 0.0723 |
| Eppler420 traditional configuration | C_{Lmax}/C_D | 38.1848 | 22.8819 |
| | α | | 17.0° |
| | C_{Lmax} | 2.5720 | 2.1106 |
| | C_D | 0.1051 | 0.1976 |
| Eppler420 high-lift configuration | C_{Lmax}/C_D | 24.4673 | 10.6822 |
| | α | | 8.0° |
| | δ | | 30.0° |
| | C_{Lmax} | 3.6850 | 2.8069 |
| NACA0015 traditional configuration | C_D | 0.07714 | 0.1049 |
| | C_{Lmax}/C_D | 47.7703 | 26.7607 |
| | α | | 5.0° |
| | C_{Lmax} | 0.6120 | 0.4582 |
| NACA0015 high-lift configuration | C_D | 0.0141 | 0.0187 |
| | C_{Lmax}/C_D | 43.2814 | 24.4410 |
| | α | | 8.0° |
| | C_{Lmax} | 0.9570 | 0.6877 |
| NACA0015 high-lift configuration | C_D | 0.0176 | 0.0560 |
| | C_{Lmax}/C_D | 54.3441 | 12.2899 |
| | α | | 9.0° |
| | δ | | 10.0° |
| NACA0015 high-lift configuration | C_{Lmax} | 1.6640 | 1.1428 |
| | C_D | 0.0300 | 0.0398 |
| | C_{Lmax}/C_D | 55.3928 | 28.7089 |

Fig. 6 shows the contour graphics corresponding to the volumetric fraction of vapor on the surface for the high-lift and traditional configuration hydrofoils. Under the studied conditions, it is observed that none of the traditional hydrofoils presented cavitation. On the other hand, in the S822 and the NACA0015 high-lift configuration hydrofoils an onset of cavitation was reached; while for the Eppler420 high-lift configuration hydrofoil, the volumetric fraction of vapor was kept at zero (without cavitation). This result can be explained from the C_p (Fig. 6) and the cavitation number calculated by using Equation (1), due to when $C_p \geq \sigma$, cavitation occurs on the hydrofoil surface.

The maximum C_p values for the traditional hydrofoil were 3.96, 3.10, 1.94 and 1.47 for the S822, Eppler420, NACA0015 (at a α equal to 8°) and NACA (at a α equal to 5°) traditional hydrofoils, respectively, as shown in Fig. 7. Additionally, the C_p values were 3.97, 4.23 and 4.23 for the Eppler420, S822 and NACA0015 high-lift configuration hydrofoils, respectively. There is a tendency to increase the C_p and the possibility of cavitation in the high-lift hydrofoil configuration. This behavior was more noticeable in the NACA0015 hydrofoil since the C_p increase in 1.47 for the

traditional configuration to values exceeding σ in high-lift hydrofoil configuration.

The greatest α values (α equal to 5° and 9° for the NACA0015 traditional and high-lift hydrofoil configurations) produce a blocking effect in the flow, generating an increase in the dynamic pressure in the hydrofoil, as well as in the forces and moments, leading to a higher pressure coefficient on the hydrofoil suction side (Cervone et al., 2006). It should be noted that the high-lift hydrofoil configuration reached a higher C_{Lmax} and a higher C_{Lmax}/C_D than the traditional hydrofoils (Table 3), allowing to obtain a better hydrodynamic performance for the high-lift hydrofoil configuration (Singh et al., 2019).

In the S822 and the NACA0015 high-lift hydrofoil configurations, it is observed that cavitation begins at the leading edge of the suction side of both hydrofoils. Cavitation is in the initiation phase, without reaching the stages of development, spilt and shedding (Ye et al., 2020).

The length of the cavitation corresponds to the flat part of the red curve in Fig. 7b and 7c. The lengths affected by the cavitation were 2.05% and 1.02% for the S822 and NACA0015 high-lift hydrofoil configurations, respectively.

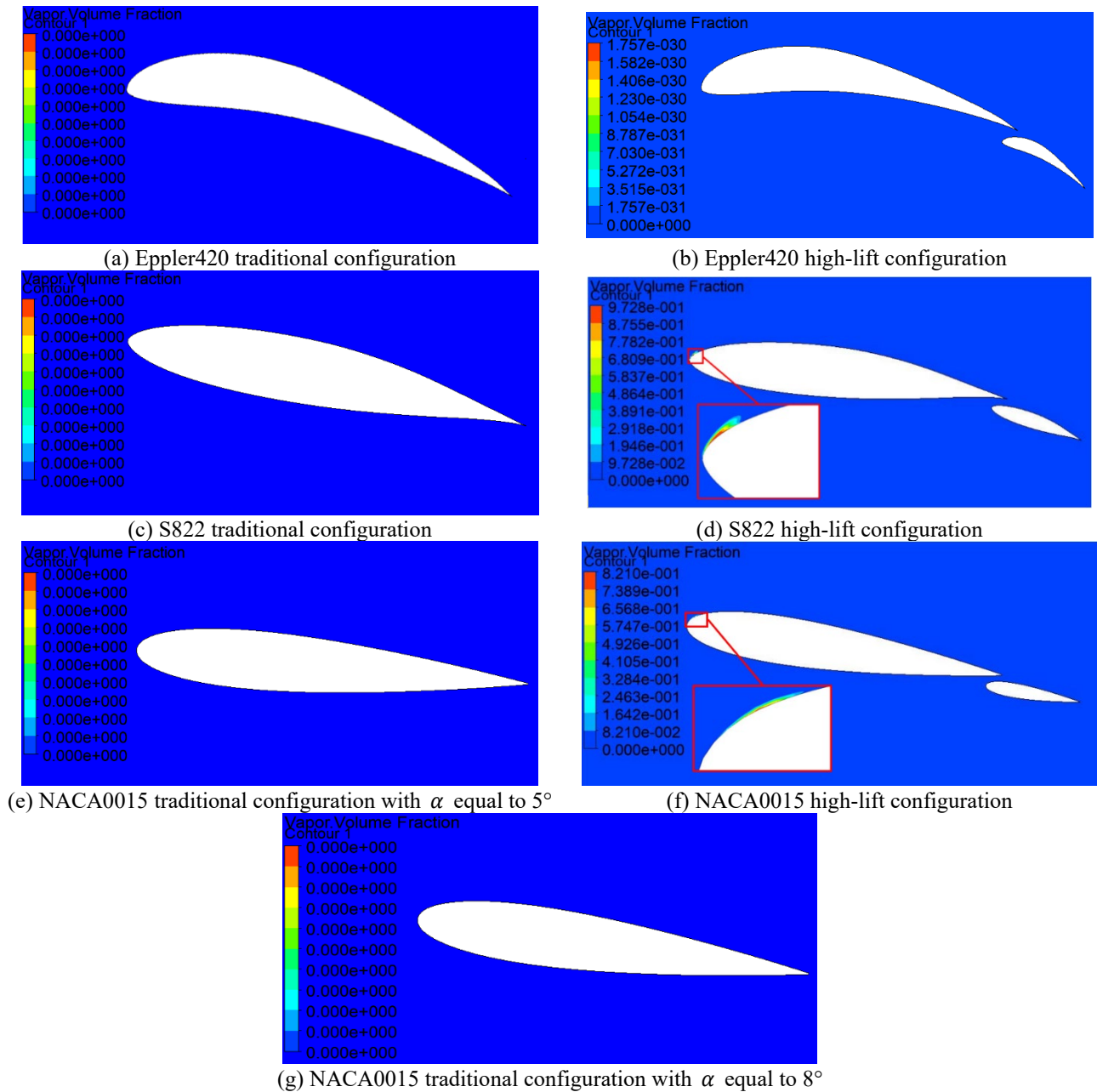


Fig. 6. Volumetric fraction of vapor for traditional and high-lift hydrofoil configuration.

Cavitation length was 1.03% greater in the S822 high-lift hydrofoil configuration compared to the NACA0015 high-lift hydrofoil configuration due to a greater pressure drop on the suction side for the S822 high-lift hydrofoil configuration (Singh et al., 2019). On the other hand, the absence of cavitation in the Eppler420 high-lift hydrofoil configuration, as well as the higher C_{Lmax} and the greater C_{Lmax}/C_D , allows this hydrofoil to be classified as the most appropriate one among the studied hydrofoils.

The results obtained by means of numerical simulation for the NACA0015 hydrofoil were validated by using the experimental results achieved by Cervone and coworkers (2006). In Fig. 7c, the experimental and numerical results

were found to be consistent and followed the same trend. The variation in the magnitude of the results is a consequence of some differences in the site conditions and variations in the configuration of the system, since in the development of the experimental work the researchers used a flow of water at a velocity value of 8 m/s, a vapor pressure equivalent to 3170 Pa (25°C) and a σ equal to 1.5 (Capurso et al., 2017; Chen et al., 2016). The experimental behavior for the traditional hydrofoils and the high-lift hydrofoil configuration would be expected to follow the same trend predicted by the cavitation model.

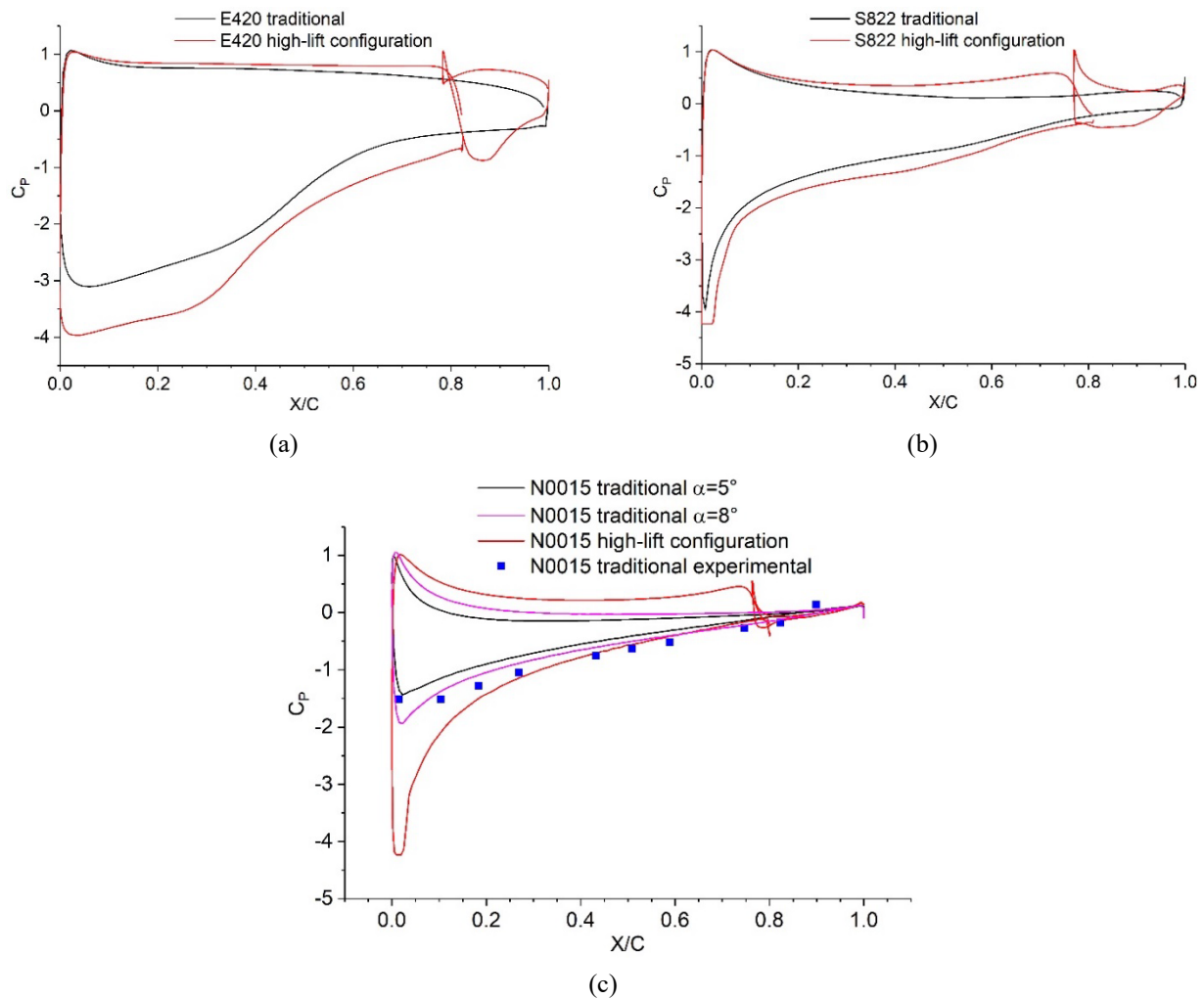


Fig. 7. C_p obtained through the numerical simulation for a) Eppler420, b) S822 and c) NACA0015 traditional and high-lift hydrofoil configurations

4. CONCLUSION

The cavitation in hydrokinetic turbine blades can cause a decrease in their performance and an eventual blade failure. Generally, cavitation can occur in those parts of the blade with high velocity, as it does in their tips. Therefore, when designing the blades of hydrokinetic turbines, selecting a hydrodynamic hydrofoil resistant to cavitation is essential. In this study, the resistance to cavitation of 3 hydrofoils was analyzed for the traditional and high-lift hydrofoil configurations by means of numerical simulations using the ANSYS Fluent software. The criterion used for the cavitation analysis of the profile consisted of comparing the C_p with σ . The results indicated that the Eppler420 high-lift hydrofoil configuration shows a good resistance to cavitation; as long as the conditions of the analysis presented for the blade studied are maintained. Therefore, its use is recommended for the hydrokinetic turbine blade design.

ACKNOWLEDGEMENT

The authors gratefully acknowledge the financial support provided by the Colombia Scientific Program within the framework of the call Ecosistema Científico (Contract No. FP44842-218-2018). Authors also acknowledge the financial support provided by Universidad de Antioquia (Estrategia de Sostenibilidad 2020-2021. ES84190067).

CONTRIBUTORS

Gutiérrez J: Methodology, Software, Writing- Original draft preparation. Rubio-Clemente A: Conceptualization, Methodology, Supervision, Writing- Original draft preparation, Funding acquisition, Resources, Project administration. Chica E: Conceptualization, Methodology, Writing- Reviewing and Editing, Funding acquisition, Resources, Project administration.

CONFLICT OF INTEREST

Gutiérrez J, Rubio-Clemente A, and Chica E declare that they have no conflict of interest.

REFERENCES

- Aguilar, J., Rubio-Clemente, A., Velasquez, L., Chica, E. 2019. Design and optimization of a multi-element hydrofoil for a horizontal-axis hydrokinetic turbine. *Energies*, 12, 4679.
- Amromin, E., Kopriva, J., Arndt, R., Wosnik, M. 2006. Hydrofoil drag reduction by partial cavitation. *Journal of Fluid Engineering*, 128, 931–936.
- Amromin, E. 2014. Design approach for cavitation tolerant hydrofoils and blades. *Journal of Fluids and Structures*, 45, 96–106.
- Batten, W.M.J., Bahaj, A.S., Molland, A.F., Chaplin, J.R. 2008. The prediction of the hydrodynamic performance of marine current turbines. *Renewable Energy*, 33, 1085–1096.
- Capurso, T., Lopez, M., Lorusso, M., Torresi, M., Pascasio, G., Camporeale, S.M., Fortunato, B. 2017. Numerical investigation of cavitation on a NACA0015 hydrofoil by means of OpenFOAM. *Energy Procedia*, 126, 794–801.
- Cervone, A., Bramanti, C., Rapposelli, E., D'Agostino, L. 2006. Thermal cavitation experiments on a NACA 0015 hydrofoil. *J. Fluids Eng. Trans. ASME*, 128, 326–331.
- Chen, T., Huang, B., Wang, G., Zhao, X. 2016. Numerical study of cavitating flows in a wide range of water temperatures with special emphasis on two typical cavitation dynamics. *International Journal of Heat and Mass Transfer*. 101, 886–900.
- da Silva, P.A.S.F., Shinomiya, L.D., de Oliveira, T.F., Vaz, J.R.P., Mesquita, A.L.A., Junior, A.C.P.B. 2015. Design of hydrokinetic turbine blades considering cavitation. *Energy Procedia*, 75, 277–282.
- Eisele, O., Pechlivanoglou, G. 2014. Single and multi-element airfoil performance simulation study and wind tunnel validation. *Wind energy impact of turbulence*. Berlin, Germany: Springer, 1722.
- Gaunaa, M., Zahle, F., Sorensen, N.N., Bak, C., Rethore, P.E. 2013. Rotor performance enhancement using slats on the inner part of a 10 MW rotor. *Proceedings of EWEA 2013—European Wind Energy Conference & Exhibition*, Vienna, Austria, European Wind Energy Association (EWEA).
- Gaunaa, M., Zahle, F., Sorensen, N.N., Bak, C. 2012. Quantification of the effects of using slats on the inner part of a 10 MW rotor. *Proceedings of EWEA 2012—European wind energy conference & exhibition*, Copenhagen, Denmark, European Wind Energy Association (EWEA).
- Gharraee, B., Eskilsson, C., Bensow, R., Vaz, G. 2016. Numerical simulation of cavitation on a horizontal axis tidal turbine. *Proceedings of the 26th International Offshore and Polar Engineering Conference, ISOPE. The International Society of Offshore and Polar Engineers ISBN 9781880653883. 709–716. Rhodes, Greece 26 Jun–1 Jul.*
- Goundar, J.N., Ahmed, M.R., Lee, Y.H. 2012. Numerical and experimental studies on hydrofoils for marine current turbines. *Renewable Energy*, 42, 173–179.
- Hong, F., Gao, Z., Yuan, J. 2018. Improvement and application of cavitation model based on Rayleigh-Plesset equation. *Journal of Agricultural Machinery*, 49, 126–132.
- Hong, F., Yuan, J., Zhou, B. 2016. Evaluation and analysis of improved Schnerr-Sauer model in hydrofoil cavitation simulation. *Journal of Harbin Engineering University*, 37, 885–890.
- Jaume, A.M., Wild, J. *Aerodynamic design and optimization of a high-lift device for a wind turbine airfoil. New results in numerical and experimental fluid mechanics X. Switzerland: Springer; 2016, 85969.*
- Jung, J.H., Kim, B.S. 2015. Rotor-blade shape design and power-performance analysis for horizontal-axis tidal turbine using CFD. *Transactions of the Korean Society of Mechanical Engineers*, 39, 661–668.
- Kim, J., Lee, J.S. 2015. Numerical study of cloud cavitation effects on hydrophobic hydrofoils. *International Journal of Heat and Mass Transfer*, 83, 591–603.
- Prakoso, A.P., Siswantara, A.I., Adanta, D. 2019. Comparison between 6-DOF UDF and moving mesh approaches in CFD methods for predicting cross-flow pico-hydro turbine performance. *CFD Letters*, 11, 86–96.
- Narsipur, A., Pomeroy, B., Selig, M. 2012. CFD Analysis of multielement airfoil for wind turbines. *30th AIAA Applied Aerodynamics Conference (2012)*. 2781.
- Ragheb, A., Selig, M. 2011. Multi-element airfoil configurations for wind turbines. In *29th AIAA Applied Aerodynamics Conference (2011)*. 3971.
- Roache, P.J. 1994. Perspective: a method for uniform reporting of grid refinement studies. *Journal of Fluids Engineering*, 116, 405–413.
- Roache, P.J. 1997. Quantification of uncertainty in computational fluid dynamics. *Annual review of fluid mechanics*, 29, 123–160.
- Sale, D., Jonkman, J., Musial, W. 2009. *Hydrodynamic Optimization Method and DesignCode for Stall-Regulated Hydrokinetic Turbine Rotors. ASME 28th International Conference on Ocean, Offshore, and Arctic Engineering Honolulu, Hawaii. 31 May to 5 June 2009.*
- Schnerr, G.H., Sezal, I.H., Schmidt, S.J. 2008. Numerical investigation of three-dimensional cloud cavitation with special emphasis on collapse induced shock dynamics. *Physics of Fluids*, 20, 040703.
- Shi, Z., Xie, Z., Shi, W., Zhang, Q., Tan, L. 2021. Numerical investigation on cavitation suppression of microchannel over a NACA0012 hydrofoil. *Shock and Vibration*, 2021, Article ID 6641839, 10, 2021.
- Singh, S., Danish, M., Saha, K. 2019. Computational investigation of cavitating flow around two dimensional

- Naca 4424 and MHKF-240 hydrofoil. *Vibroengineering Procedia*, 29, 159–164.
- Wang, S., Sheng, C., Yuan, P., Tan, J., Zhang, K. 2015. Numerical simulation of cavitation on horizontal axis tidal current turbine. *Taiyangneng Xuebao/Acta Energetica Solaris Sinica*, 36, 522–528.
- Yavuz, T., Koç, E., Kılış, B., Erol, Ö., Balas, C., Aydemir, T. 2015. Performance analysis of the airfoil-slat arrangements for hydro and wind turbine applications. *Renewable energy*, 74, 414–421.
- Ye, W., Yi, Y., Luo, X. 2020. Numerical modeling of unsteady cavitating flow over a hydrofoil with consideration of surface curvature,” *Ocean Eng.*, 205, March, 2020.
- Zahle, F., Gaunaa, M., Sorensen, N.N., Bak, C. Design and wind tunnel testing of a thick, multi-element high-lift airfoil. *Proceedings of EWEA 2012—European Wind Energy Conference & Exhibition, Copenhagen, Denmark, European Wind Energy Association (EWEA); 2012.*
- Zhang, L., Fang, L., Zhang, X. 2015. Study on cavitation characteristics of horizontal axis tidal turbine. *Huazhong Keji Daxue Xuebao (Ziran Kexue Ban)/Journal of Huazhong University of Science and Technology (Natural Science Edition)*, 43, 50–54.